Chemical routes to materials

Experimental and DFT-D3 study of sensitivity and sensing mechanism of ZnSnO$_3$ nanosheets to C$_3$H$_6$O gas

Lili Jiang[1,*] , Zhaoyu Chen[1], Qi Cui[1], Su Xu[1], and Fuling Tang[1]

[1] *School of Material Science and Technology, Lanzhou University of Technology, Langongping Road, Lanzhou 730050, Gansu Province, China*

ABSTRACT

To find a new type of sensing material with high sensitivity to acetone gas, in this paper, a first-principles method based on density functional theory was used to study the gas-sensing mechanism of perovskite-type ZnSnO$_3$ to acetone. A hydrothermal method was used to prepare perovskite-type ZnSnO$_3$, and perform a gas sensitivity test. Calculated results demonstrate that acetone molecules interacted strongly with the ZnSnO$_3$(001) surface with pre-adsorbed O$_2^-$ and O$^-$, accompanied by charge transfer that can change the resistance of the material. This phenomenon provides the basis for using ZnSnO$_3$ as an acetone gas-sensitive sensing material. The experimental results showed that the perovskite-type ZnSnO$_3$ has a sheet structure with micro-holes on the surface, which can promote responsivity to acetone gas. The gas sensitivity test indicated the optimal operating temperature is 350 °C, the response/recovery time is 4 s/27 s. The sensitivities of the synthesized ZnSnO$_3$ nanosheet that in this paper to 100 ppm and 10 ppm acetone gas are 125.444 and 8.37, respectively. In the five-week stability and repeatability test, the sensitivity to 10/100 ppm acetone of sheet-like ZnSnO$_3$ sensor could still maintain at 89.64% and 94.74% of the first test result. This study provides theoretical guidance for the development of acetone gas sensors.

Introduction

Acetone is a common volatile organic compound (VOC) that is widely used in chemical and biological industries [1]. Exposure to acetone gas is common in daily life, such as through painting, plastic, and decorative panels [2]. Acetone is very chemically active and highly volatile at room temperature. Inhalation of acetone gas can cause nausea, headache, fatigue, and other symptoms, and in large quantities, even coma [3]. Medical studies show that the acetone

Address correspondence to E-mail: jianglili2002@163.com
E-mail Addresses: s541040349@163.com; cq2523305817@163.com; 769457904@qq.com; tfl@lut.edu.cn

🙋 Springer

concentration in the exhaled breath of diabetic patients is typically more than twice that of healthy people, making the acetone concentration a test indicator of diabetes [4]. Therefore, it is necessary to detect and monitor acetone gas.

With the continuous development of sensor technology, gas sensors have become one of the effective methods for detecting harmful gases [5–7]. Recently, since metal oxide semiconductor (MOS) gas sensors have the advantages of simple synthesis, low cost, and low energy consumption, the research on such gas sensors have attracted widespread extensive attention. The sensors based on MOS mainly include simple metal oxides type (such as SnO_2 [4, 8], WO_3 [9], NiO [10], In_2O_3 [11], CuO [12]) and perovskite oxides type (such as $LaFeO_3$ [13], $LaMnO_3$ [14], $SmFeO_3$ [15], $ZnSnO_3$ [16]). Compared to the simple metal oxides materials, perovskite oxides with an ABO_3 structure not only have high sensitivity to harmful gases but also have strong thermal stability and controllability at a low preparation cost [17–23]. Thus perovskite oxide is a promising candidate for fabricating gas sensors. Balamurugan et al. used a hydrothermal method to synthesize $GdFeO_3$ with a high specific surface area, which showed a high response rate of 91% for 100 ppm NO [24]. Mohammed et al. used high-energy ball milling to prepare nanocrystalline $LaCoO_3$, which exhibited excellent gas sensitivity to CO, and the responsivity could be improved through additional milling steps [25]. Chaudhari et al. used a sol–gel method to synthesize a $LaFeO_3$-based gas-sensing material, which exhibited good sensitivity to NH_3, modifying $LaFeO_3$ by Co-doping reduced the detection temperature for NH_3 from 260 to 200 °C [26]. Chen et al. used a sol–gel method to prepare $LaCrO_3$ nanocrystals. The sensitivity of these nanocrystals to CO_2 gas at high temperatures was investigated, and first-principles methods were used to explain the gas-sensing mechanism [27]. Density functional theory (DFT) becomes one of the most efficient methods to investigate the surface adsorption reaction mechanism for gas molecules [28]. Li et al. used DFT to model the oxidation mechanism of NO on the surface of undoped and Ce-doped $LaCoO_3$ (011). The results showed that Ce doping could improve the activity of the material surface to NO [29]. Wu et al. found that the adsorption energy of a $LaFeO_3$ surface to CO could be considerably increased by Ca doping and

the presence of oxygen vacancies using DFT method [30].

The perovskite-type metal oxide $ZnSnO_3$ was studied because the excellent is characterized by a high electron transfer rate and chemical response and has shown excellent performance [31–33], especially in terms of good gas sensitivity to harmful gases. Xu et al. used a one-step hydrothermal method to synthesize $ZnSnO_3$ particles and found that a $ZnSnO_3$-based sensor had good sensitivity and selectivity to H_2S gas [34]. Guo et al. prepared $ZnSnO_3$ hollow nanocages that exhibited good gas sensitivity to HCHO, with a response and recovery times reaching 3 s and 5 s, respectively [35]. Parmeshwar et al. prepared cubic $ZnSnO_3$ hydrothermal method to detect H_2 gas, the results indicating that cubic $ZnSnO_3$ Sensor exhibits rapid response (~ 1 s), fast recovery (~ 12 s), and good selectivity to H_2 [36]. However, few studies have been conducted on the $ZnSnO_3$ nanosheet and gas-sensing mechanism to acetone so far.

A first-principles method based on DFT was used to perform a detailed investigation of the gas sensitivity and gas-sensing mechanism of perovskite-type metal oxide $ZnSnO_3$ in this study. Analyses were performed on the adsorption energy, charge-density difference (CDD), density of state (DOS), partial density of state (PDOS), and Bader charge. Experiments were performed next. A hydrothermal method was used to prepare the $ZnSnO_3$ gas-sensitive material, which was subsequently characterized using X-ray diffraction (XRD), transmission electron microscopy (TEM), high resolution transmission electron microscope (HRTEM), energy dispersive X-ray spectroscopy (EDX), and scanning electron microscopy (SEM). The material was finally subjected to a gas sensitivity test. This study provides theoretical guidance for the development of high-performing acetone gas sensors.

Methodology

Model and computational details

The Vienna Ab-initio Simulation Package (VASP) was used to perform DFT-D3 calculations [37]. The generalized gradient approximation (GGA)-Perdew-Burke-Ernzerhof (PBE) function [38, 39] was selected to describe the electron interactions. A cutoff energy

test showed that the energy of the system did not change significantly at cutoff energy of 520 eV, which was therefore selected as the cutoff energy. The Monkhorst–Pack method was used to perform the structural optimization, a $1 \times 5 \times 1$ k-point grid was used to describe the Brillouin zone, and a $5 \times 5 \times 1$ k-point grid was used for the self-consistent and non-consistent calculations. The geometrical structure optimization was performed using an energy convergence criterion of 1×10^{-5} eV and a force convergence criterion of -0.01 eV/Å. The DFT-D3 method was used to correct the van der Waals force [40, 41], and the VASPKIT software package was used for data post-processing [42].

As the crystal structure of perovskite-type metal oxides is well known to change with increasing temperature, perovskite semiconductor gas-sensitive materials typically exhibit gas sensitivity at high temperatures [27]. Calculations were performed on the orthorhombic structure of $ZnSnO_3$ at a high temperature (pnma (62) space group) [43] (the lattice constants were $a = 5.381$ Å, $b = 5.408$ Å, and $c = 7.940$ Å) with 20 atoms in the unit cell to ensure high consistency between the theoretical calculation and experimental results. The C_3H_6O and O_2 molecules used in this calculation were structurally optimized. The C=O, C–H, and C–C bond lengths in the C_3H_6O molecule were 1.22 Å, 1.51 Å, and 1.095 Å, respectively, with calculation errors of 0%, 0%, and 0.6%, respectively [44]. The O=O bond length in the O_2 molecule was 1.23 Å, and the calculation error was 0.8% [45]. These results showed that the gas molecule model used in the calculation was reasonable.

The adsorption energy (E_{ads}) is an important criterion for determining whether an adsorption reaction can proceed spontaneously. Equation (1) was used to calculate energy E_{ads}:

$$E_{ads} = E_{surface+gas} - \left(E_{surface} + E_{gas}\right) \quad (1)$$

where $E_{surface+gas}$ represents the total energy of the adsorption system in equilibrium, $E_{surface}$ represents the surface energy, and E_{gas} represents the total energy of the gas molecules. Endothermic and exothermic adsorption reactions are indicated by $E_{ads} > 0$ and $E_{ads} < 0$, respectively. In this paper, the zero-point energy (ZPE) correction and thermal correction were carried out. The ZPE of gas molecules was carried out by the calculation of vibrational frequency, and the thermal correction of the free and

adsorbed gas molecules is carried out through the VASPKIT software package at the standard conditions (298.15 K, 1 atm) and 623.15 K, 1 atm.

CDD plots were used to elucidate the electron interaction and charge transfer between the gas molecule and the adsorbent (Eq. (2) [46]):

$$\Delta\rho = \rho_{surface+gas} - \rho_{surface} - \rho_{gas} \quad (2)$$

where $\Delta\rho$ is the change in the total charge density and $\rho_{surface + gas}$, $\rho_{surface}$, and ρ_{gas} are the total charge densities of the adsorption structure, adsorption surface, and adsorbed molecules, respectively.

A Bader charge analysis was used to analyze the charge transfer between the acetone gas molecule and the surface during the reaction to elucidate the reaction mechanism.

Experimental methods

Preparation and characterization of $ZnSnO_3$

0.8 g of zinc acetate dihydrate ($ZnCH_3COOH \cdot 2H_2O$) and 0.659 g of sodium stannate ($Na_2SnO_3 \cdot 3H_2O$) were added to 30 mL of distilled water and magnetically stirred for 10 min to completely dissolve them. The samples were marked as solutions A and B. Solution A was added to solution B drop wisely. After 40 min of magnetic stirring, the mixture was transferred to a polytetrafluoroethylene reactor, which was placed in a vacuum drying oven at 160 °C for 12 h. After this process is completed, the sample is washed with distilled water and dried. The white powder was calcined in a tubular furnace at 550 °C under an argon atmosphere for 3 h to produce sheet-like $ZnSnO_3$.

The crystal structure of $ZnSnO_3$ was analyzed by XRD (D8/AXS, Bruker, Germany) using Cu kα radiation at room temperature. The morphology of the prepared nanomaterials was studied by SEM (model JSM-7600F, JEOL) and TEM (model JEM-2010, JEOL). Finally, a CGS-4TPs intelligent gas-sensing analysis system was used (Beijing Elite Tech. Co., Ltd.) to conduct a gas sensitivity test on $ZnSnO_3$.

Gas-sensitivity testing

A small quantity of $ZnSnO_3$ was placed in a mortar and ground evenly. An appropriate amount of anhydrous ethanol was then added to form a paste that was applied evenly to an interdigitated gold

electrode. The coated electrode was placed in a constant-temperature drying oven at 80 °C for 8 h. The dried electrode was placed in the gas-sensing test system. A five-volt voltage was applied, and the test electrode was obtained after 12 h of aging at 200 °C. The sensor sensitivity is defined in Eq. (3):

$$S = Ra/Rg \tag{3}$$

where Ra and Rg denote the resistance (Ω) of the material in air and in the target gas, respectively. The response time (T_{res}) is defined as the time required for the material to reach 90% of the maximum sensitivity under the target gas atmosphere, and the recovery time (T_{rec}) is defined as the time required for the material to reach 90% of the original resistance under no target gas atmosphere.

Results and discussion

Selection of the most stable surface

The (001), (100), and (010) surfaces of the $ZnSnO_3$ crystal were selected as candidate adsorption surfaces. A 15 Å vacuum layer was inserted between the layers to prevent interactions. Equation (4) was used to calculate the surface energy of the three surfaces, and the most stable surface was selected [47].

$$\gamma = \frac{E_{slab} - n \cdot E_{bulk}}{2A} \tag{4}$$

In the equation above, γ represents the surface energy, E_{slab} represents the total surface energy, E_{bulk} represents the total energy of the unit cell, n is the number of unit cells contained in the surface, and A is the surface area. The smaller the surface energy is, the more stable the surface is.

The results of the surface energy calculation for the different surfaces are shown in Fig. 1. With the lowest surface energy, the (001) surface is the most stable in the perovskite $ZnSnO_3$ structure. The (001) surface has two types of terminations, Sn–O end and Zn–O end. Calculated single point energy of the end surfaces showed that the Sn–O end was the more stable and was, therefore, used in subsequent calculations. Figure 2 shows that the Sn–O end of the (001) surface expanded into a 3 × 1 supercell (a = 15.93 Å, b = 5.33 Å, and c = 20.33 Å) with four-layer atoms in the supercell and alternating Sn–O and Zn–O layers. In the calculation, the bottom two layers of atoms are
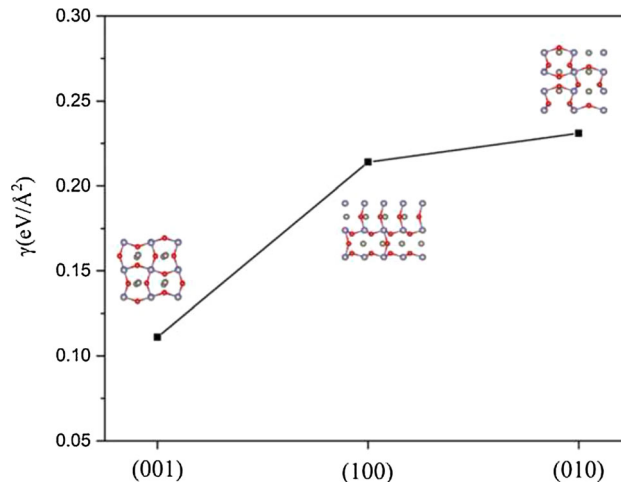

Figure 1 The surface energies of (100), (010), (001) surfaces of cubic $ZnSnO_3$, red = Oxygen atom, gray = Zn atom, white = Sn atom.

fixed, and only the top two layers of atoms are relaxed. Three initial adsorption sites, namely, O-top, Sn-top, and Hollow-top, were considered in subsequent calculations (Fig. 2b).

Adsorption of acetone molecules by a clean $ZnSnO_3(001)$ surface

First, the adsorption of acetone molecules on a clean $ZnSnO_3$ (001) surface without pre-adsorbed oxygen was studied in a vacuum. Figure 3 shows the three initial adsorption sites on the surface of $ZnSnO_3(001)$ that were considered. The acetone molecules approach the surface with the O^- end facing down at these sites. For all three adsorption optimized structures after structural optimization, the acetone molecules are adsorbed on the surface with the O end close to the Sn atom. The E_{ads} and charge transfer capacity of these structures are shown in Table 1.

Table 1 shows that the E_{ads} of the three adsorption structures are all less than zero, indicating that the adsorption of acetone molecules on the clean $ZnSnO_3(001)$ surface is exothermic and spontaneous process. The Bader charge analysis results for all three adsorption structures show that acetone molecules capture electrons from the surface, and the $ZnSnO_3(001)$ surface loses 0.021 e, 0.016 e, and 0.008 e electrons. The small transferred charge indicates that the adsorption of acetone molecules on the clear $ZnSnO_3(001)$ surface is a physical adsorption process dominated by van der Waals forces. $ZnSnO_3$ is an

Figure 2 **a** The side view of clean ZnSnO₃ (001) surface, Red = Oxygen atom, gray = Zn atom, white = Sn atom, **b** three Initial adsorption sites.
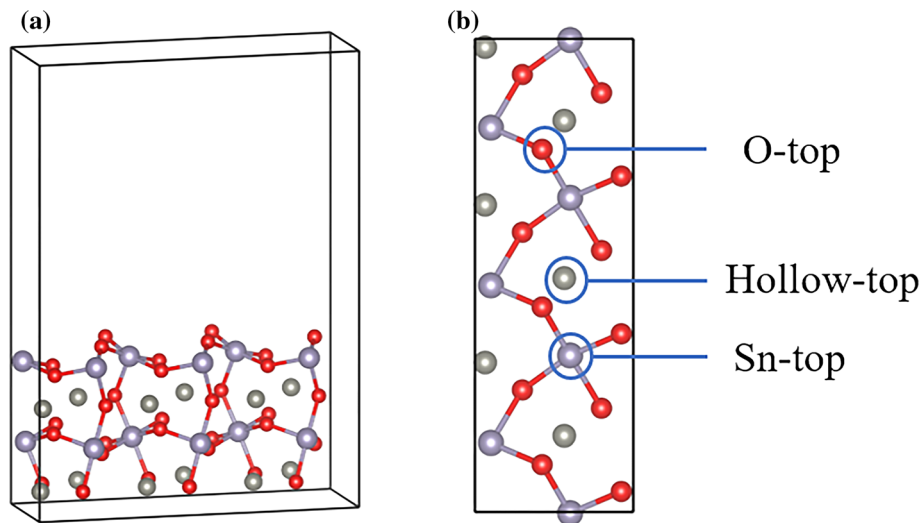

Figure 3 The configuration of molecular acetone adsorption on ZnSnO₃(001) surface. The left part is before optimizing the structure, the right part is after optimizing the structure. (T1) O end down at Sn site; (T2) O end down at O site; (T3) O end down at hollow site.
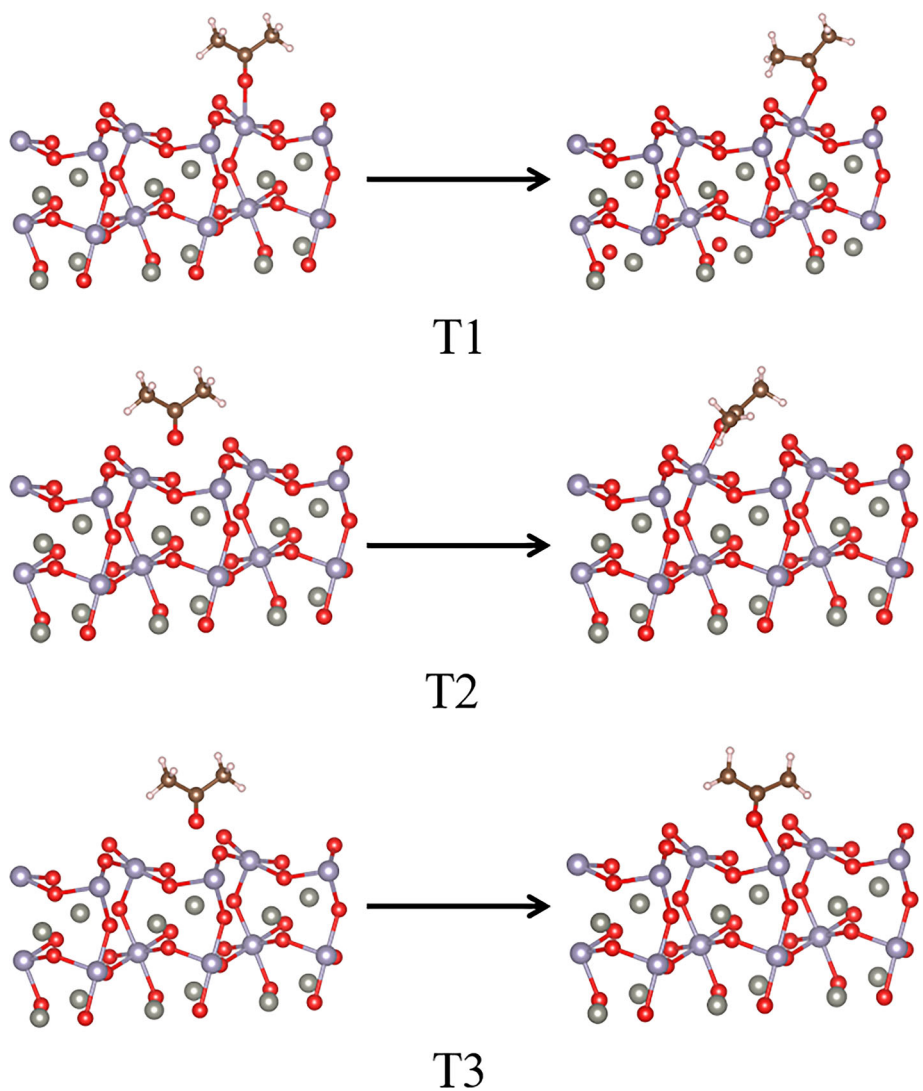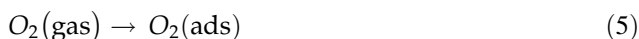
Table 1 Properties of the adsorption acetone molecular on the $ZnSnO_3(001)$ surface at the standard condition

	E_{ads} (eV)	Surface charge transfer (e)
T1	− 0.19	− 0.021
T2	− 0.34	− 0.016
T3	− 0.1	− 0.008

n-type semiconductor in which electrons act as carriers [41]. The calculation results show that during the adsorption process, acetone molecules act as charge acceptors, and $ZnSnO_3$ materials act as charge donors. The adsorption of acetone molecules causes a decrease in the carrier concentration and an increase in resistance. This result is contrary to the experimental observations. Therefore, the clean $ZnSnO_3(001)$ surface model could not be used to analyze the response mechanism of the $ZnSnO_3$ gas-sensitive material to acetone gas.

In the working environment of a gas sensor, the gas-sensitive material first adsorbs oxygen in the air to form O_2^- ions on the surface before contacting the target gas that decomposes into O^- as the temperature increases. This reaction is shown in Eqs. (5)-(7) [45].

$$O_2(gas) \rightarrow O_2(ads) \tag{5}$$

$$O_2(ads) + e^- \rightarrow O_2^-(ads) \tag{6}$$

$$O_2^-(ads) \rightarrow 2O^-(ads) \tag{7}$$

Therefore, a model for the $ZnSnO_3(001)$ surface with pre-adsorbed O (O_2^- and O^-) was established to increase the consistency between the calculation model and experimental results.

Pre-adsorption of O_2 molecules on the $ZnSnO_3(001)$ surface

Three adsorption sites are considered for the adsorption of O_2 molecules on the $ZnSnO_3(001)$ surface. Two initial adsorption configurations are considered for each adsorption site corresponding to O_2 molecules perpendicular and parallel to the surface. The distance between an O_2 molecule and the surface is 2.5 Å. The structures before and after optimization are shown in Fig. 4. In this section, the E_{ads} was corrected at standard condition.

Comparing the N1-N4 models presented in Fig. 4 with the initial adsorption structure shows that the optimized O_2 molecules are close to the $ZnSnO_3(001)$ surface and tend to approach the Sn sites of the surface. However, the O_2 molecules are far from the $ZnSnO_3(001)$ surface in the N5 and N6 adsorption structures. Table 2 provides the E_{ads} of the adsorption structures for N1-N6, as well as the changes in the O=O bond length and the transferred charge of the O_2 molecules. The E_{ads} of the N1-N4 models shown in Table 2 is all less than zero, indicating that the adsorption reactions proceed spontaneously for these models. By comparison, the adsorption energies of N5 and N6 are small (− 0.04 eV and 0.01 eV, respectively), where the adsorption reaction in N6 is endothermic and not spontaneous. Structural optimization changes the O=O bond length for N1-N4 by 0.016 Å, 0.017 Å, 0.043 Å, and 0.041 Å, whereas no significant changes were observed for N5 and N6.

The DOS plots of adsorbed and free O_2 for models N1-N6 were compared to elucidate the adsorption mechanism of O_2 on the surface. In Fig. 5, the DOS plots of O_2 in N5-N6 are very similar to that of free O_2, and only positional differences can be observed. Thus, there is no change in the O=O bond in the O_2 molecules in these two adsorption structures. In the DOS plots of O_2 for N1-N4, the peak at the Fermi level shifts to the low energy side, and distinct peak splitting and dispersion occur at − 6.5 eV and near the Fermi level, suggesting the occurrence of chemical reactions between O_2 and the surface. N1 and N3 were selected as representative models to perform a PDOS analysis, and the results are shown in Fig. 6. The complete overlap between the p orbitals of O_2 and Sn near the Fermi level indicates a strong chemical reaction between the Sn ion and O_2. Figure 6b shows similar adsorption for N3 and N1. The Bader charge analysis (Table 2) shows that O_2 captures electrons from the surface during chemical adsorption, and the obtained electrons are mainly distributed on the O atoms close to the surface. The results show that O_2 is most easily adsorb on the $ZnSnO_3(001)$ surface at the Sn-top and hollow-top sites of the surface and eventually adsorb on the Sn site, O_2 captures electrons from the surface to form the O_2^- ion during the adsorption process. This stable chemical adsorption provides favorable conditions for the dissociation of oxygen on the surface and the chemical reaction with the target gas.

The phenomenon of O_2 capturing electrons from the surface is consistent with the experimental observation that n-type semiconductors react with

Figure 4 The configuration of molecular oxygen adsorption on $ZnSnO_3$ (001) surface; the left are before optimizing the structure; the right are after optimizing the structure; the oxygen molecule is perpendicular to the Sn site (N1); the oxygen molecule is parallel to the Sn site (N2); the oxygen molecule is perpendicular to the hollow site (N3); the oxygen molecule is parallel to the hollow site (N4); the oxygen molecule is perpendicular to the O site (N5); the oxygen molecule is parallel to the O site (N6).
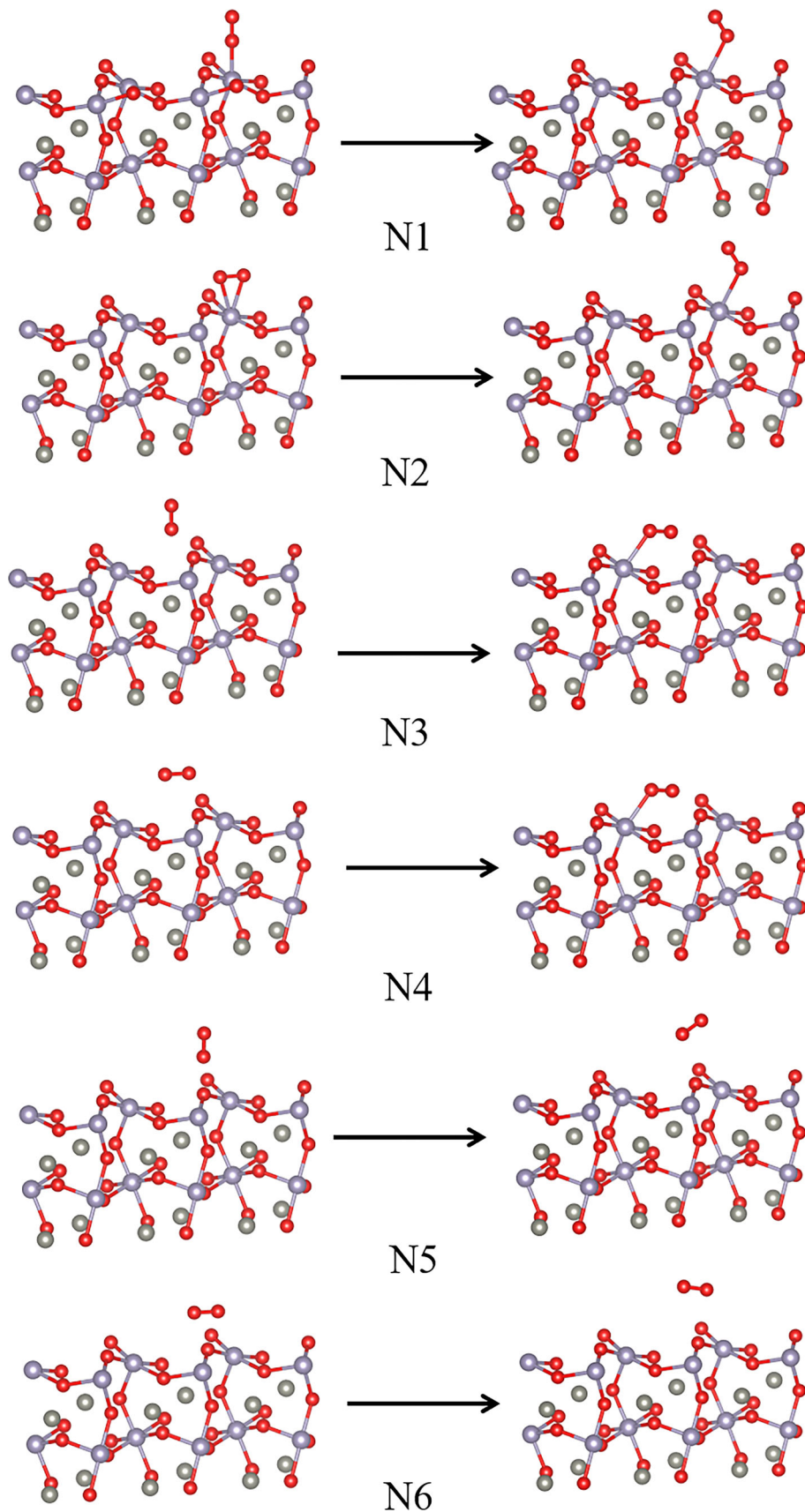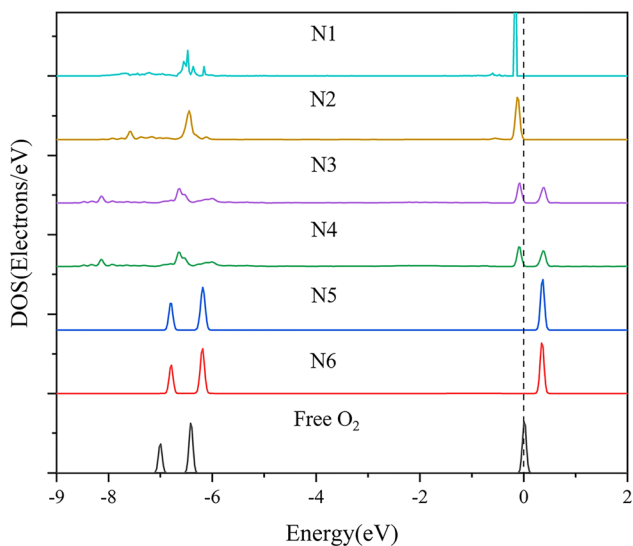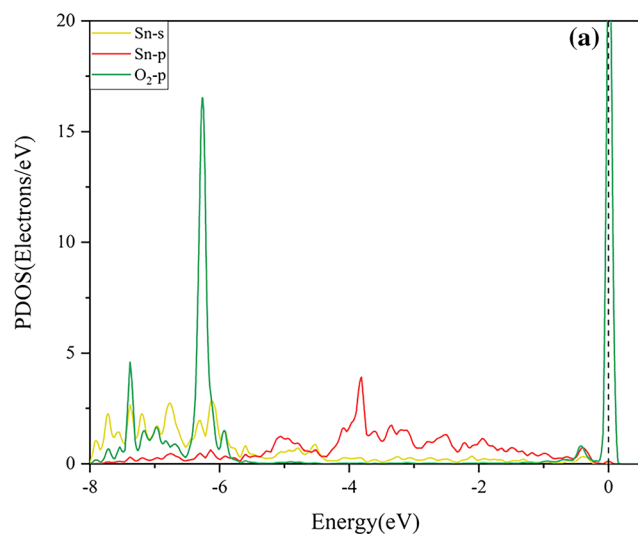
Table 2 Properties of the adsorption oxygen molecular on the ZnSnO$_3$(001) surface

	E_{ads}(eV)	d_{o-o}(Å)	Charge transfer of O$_2$ (e)
N1	− 0.249	1.250	+ 0.126
N2	− 0.231	1.251	+ 0.128
N3	− 0.471	1.277	+ 0.127
N4	− 0.469	1.275	+ 0.183
N5	− 0.04	1.235	+ 0.015
N6	0.01	1.235	+ 0.015

Figure 5 The DOS of free O$_2$ and adsorbed O$_2$ in model N1-N6.

Figure 6 PDOS of model N1 and N3, **a** N1; **b** N3.

oxidizing gases. Therefore, the surface with an O$_2$ molecule adsorbed on an Sn-top site was used as the surface with pre-adsorbed O in subsequent calculations.

Interaction between the ZnSnO$_3$(001) surface with pre-adsorbed O$_2^-$ and acetone gas

The interaction between the ZnSnO$_3$(001) surface with pre-adsorbed O$_2^-$ and acetone gas molecules was studied to elucidate the adsorption mechanism. The five initial adsorption structures shown in Fig. 7 were considered. As Fig. 7 shows, after structural optimization of models M1 and M2, the acetone molecules lie far from the ZnSnO$_3$(001) surface, which indicates that an upward-pointing O end does not facilitate adsorption of acetone molecules. Structural optimization of models M3 and M4 results in the acetone molecules being close to the ZnSnO$_3$(001) surface, where the O end tends to approach the Sn ion on the surface. In M4, the pre-adsorbed O$_2^-$ dissociate from the surface under the influence of the acetone molecules. M5 structure indicates that the oxygen molecules dissociate on the surface(the distance between O atoms changed from 1.23 to 1.47 Å), and one of which connects to the C atom in the carbonyl group of acetone to form methyl acetate, which
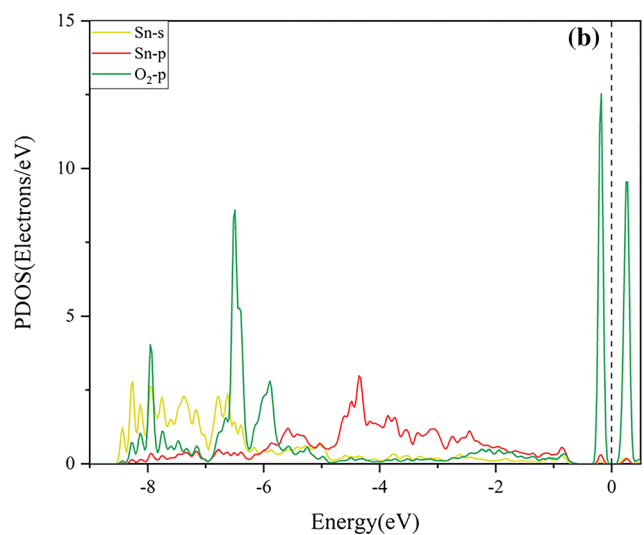
Figure 7 The configuration of molecular acetone adsorption on ZnSnO$_3$ (001) surface of pre-adsorbed O$_2$. The left are before optimizing the structure. The right are after optimizing the structure.(M1) The O end upward and the H end is close to the pre-adsorbed oxygen; (M2) The O end upward and the carbon atom is close to the pre-adsorbed oxygen; (M3) The acetone is parallel to the surface and the H end are close to the pre-adsorbed oxygen; (M4) The acetone is parallel to the surface and the O end are close to the pre-adsorbed oxygen; (M5) The O end down and the carbon atom is close to the pre-adsorbed oxygen.

M1

M2

M3

M4

M5
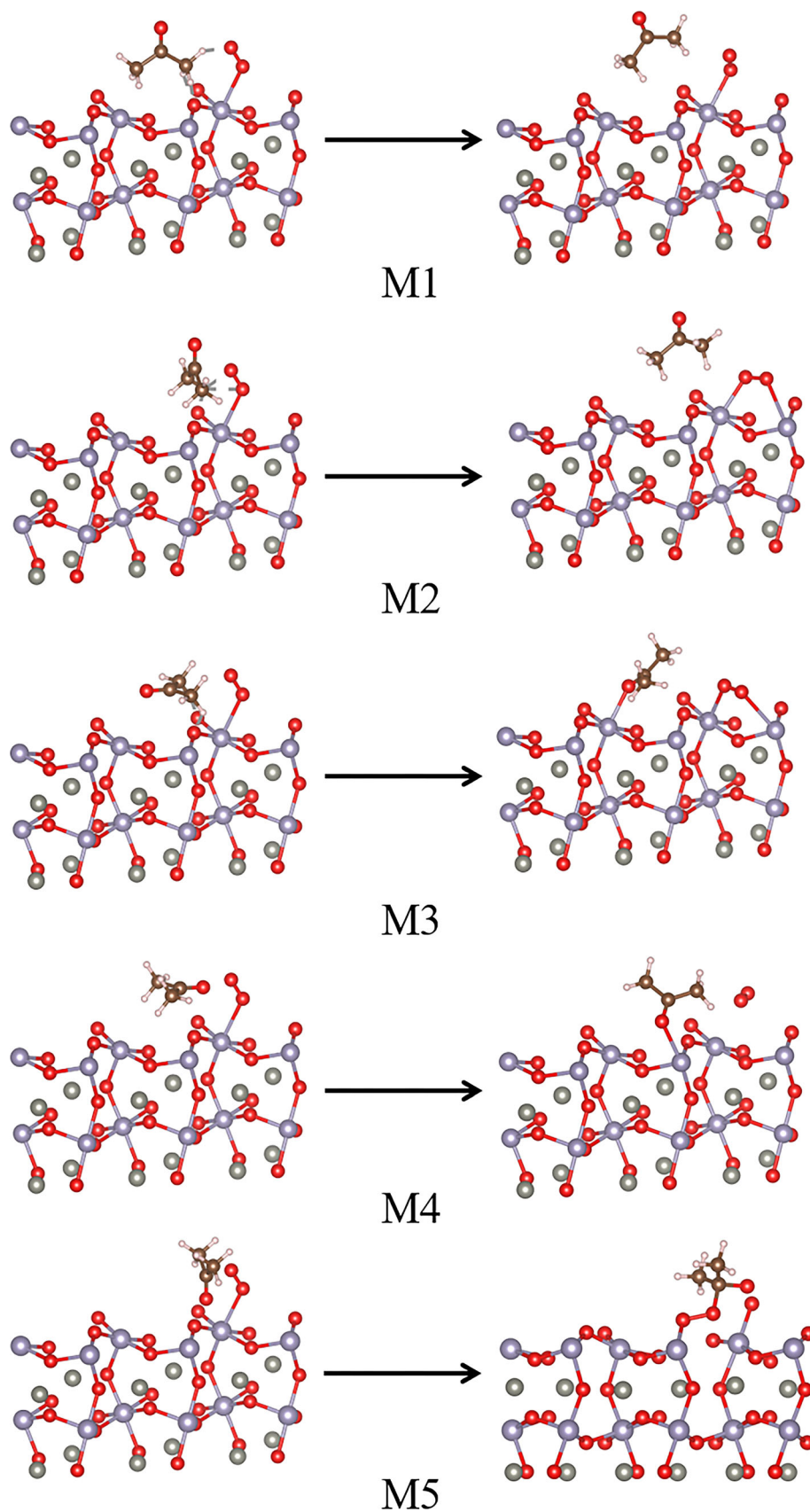
is consistent with the results reported in the Ref. [46]. Cleavage of the Sn–O bond also occurs in M5.

In the DOS plots of the acetone molecules in M1-M5 presented in Fig. 8. In M1 and M2, the peak of acetone is shifted to the low-energy side with no apparent split compared to the DOS for free acetone molecules, this indicates that the interaction between the acetone molecule and the surface in M1 and M2 is relatively weak. The DOS plots of acetone for M3 and M4 shift to the low energy side, and distinct structural changes occur, indicating that gas molecules in M3 and M4 are chemically adsorbed to the surface. At the same time, the high similarity of the peak shapes (Fig. 8) indicates that similar adsorption reactions occur in M3 and M4. In the M5 structure, the DOS peak of the acetone molecule has the strongest dispersion, indicating that is a strong interaction between gas molecules and the surface. The distinct changes in the peak structure in the DOS plot of acetone molecules in models compared with that of free acetone molecules may be caused by charge transfer.

Table 3 shows the E_{ads} for M1-M5 at different temperatures and the transferred charge of the acetone molecules. At 298.15 K, 1 atm condition, the E_{ads} of M1-M4 structures are all less than 0, the E_{ads} of M5 structure is bigger than 0, indicating that the reactions in M1-M4 can proceed spontaneously, while the adsorption reaction in M5 is non-spontaneous and endothermic. At 623.15 K, 1 atm condition, all adsorption reactions can proceed spontaneously, and
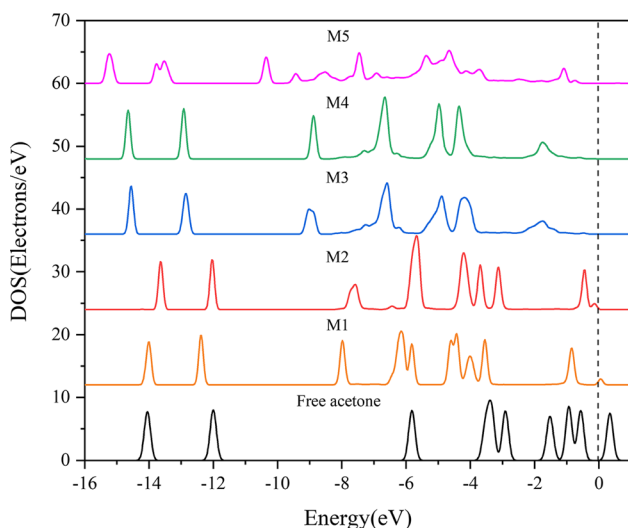
the absolute value of E_{ads} is greater than under standard conditions, which indicates that the high temperature, adsorption reactions are more likely to occur and the adsorption structure is more stable. The Bader charge analysis (Table 3) shows that in M1-M5 structures, the surface is the electron acceptor and the acetone molecule is the electron donor. As know the absolute value of the E_{ads} increases with the charge transfer in M1-M4. But in the M5 adsorption structure, acetone molecules provide a charge of 0.544 e to the surface, indicating strong and stable chemical adsorption of acetone molecules by this structure. But the E_{ads} results show that compared with M3 and M4, the adsorption reaction in M5 can only occur at high temperatures.

Models M4 and M5 were selected for CDD and PDOS analyses to elucidate the adsorption mechanism of acetone molecules on the surface with pre-adsorbed O. Figure 9 shows the CDD plots for M4 and M5, where the blue and yellow areas correspond to charge divergence and convergence, respectively. In Fig. 9a, charge transfer mainly occurs inside the carbonyl group and between the acetone O and the Sn on the surface (in M4, the C atom in the carbonyl group loses a charge of 0.89 e and becomes positively charged, whereas the O atom gains a charge of 1.11 e to become negatively charged). And the pre-adsorbed O_2 molecules at the surface are dissociated and, therefore, transfer almost no charge to the surface. Figure 9b shows that charge transfer mainly occurs inside the carbonyl group of the acetone molecule and between the acetone molecule and the active lattice O on the surface. When acetone is adsorbed on the ZnSnO$_3$(001) surface, charge transfer occurs between C=O bonds of the carbonyl group. An electrophilic positively charged C center and a nucleophilic negatively charged O center are generated because the O atom in the carbonyl group is more electronegative than the C atom. An electrophilic (nucleophilic) substance reacting with acetone will preferentially attack the O atom (C atom) in the carbonyl group. Therefore, the following mechanism is proposed for acetone adsorption in M3 and M4. The negatively charged O center in the carbonyl group of the acetone molecule undergoes a nucleophilic reaction with the Sn ion on the surface and is adsorbed on the surface through a lone electron pair. In M5, the active lattice oxygen first reacts with the acetone, generating an acetone-oxygen complex. At the same time, the pre-adsorbed O_2 molecule pre-

Figure 8 The DOS of free acetone and adsorbed acetone in M1-M5.

Table 3 Properties of the adsorption acetone molecular on the ZnSnO$_3$(001) surface of pre-adsorbed O$_2$

Model	E_{ads}(eV)		Charge transfer of C$_3$H$_6$O (e)
	298.15 K, 1 atm	623.15 K, 1 atm	
M1	− 0.302	− 0.792	− 0.016
M2	− 0.419	− 0.909	− 0.016
M3	− 0.791	− 1.261	− 0.076
M4	− 0.933	− 1.403	− 0.089
M5	0.224	− 0.366	− 0.544
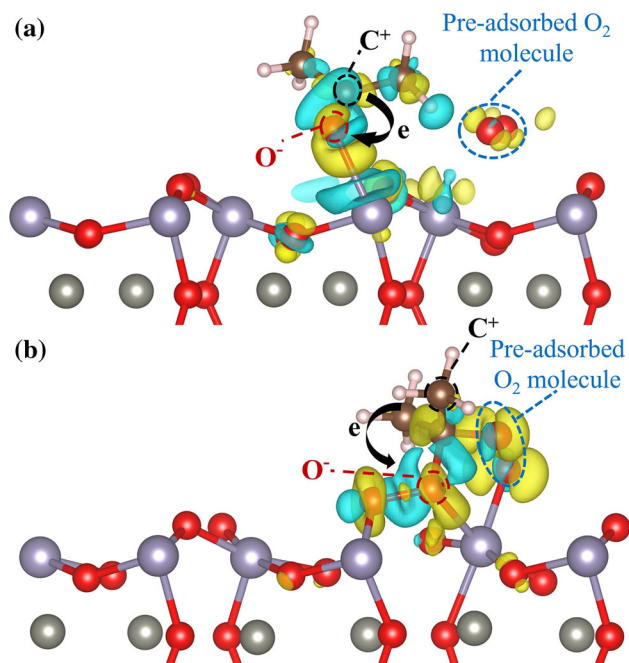
Figure 9 The CDD of M4, M5. Blue represents the region of charge divergence, yellow represents the region of charge convergence. **a** M4, **b** M5. The isosurfaces refer to isovalues of 1×10^{-3} electrons/bohr^3.

adsorbed on the surface dissociates, and an O atom attacks the positively charged C center of the carbonyl group in acetone, causing the acetone-oxygen complex to be oxidized [13]. The reaction of the active lattice O on the surface with the acetone forms an O vacancy. This vacancy is filled by the O atom that does not participate in the reaction after the dissociation of O$_2$ molecules and adsorbs at the Sn site on the surface. This consumption-replenishment process conforms to the Mars-van Krevelen (MvK) mechanism [29].

Figure 10 shows the PDOS of M4 and M5. Figure 10a shows the PDOS plots of O atoms in acetone and surface Sn atoms in M4. The adsorption of acetone molecules at the Sn site on the ZnSnO$_3$(001) surface results in strong hybridization between the

O-p orbital and Sn-p orbital in acetone near the Fermi level, indicating that the bonding between Sn–O is mainly caused by hybridization between the p orbitals of Sn and O. The PDOS plots of the O atom in acetone and the O atom in the broken Sn–O bond on the surface of M5 (Fig. 10b) show peak overlap between the p orbitals of the acetone O atom and the surface O near the Fermi level and at a low energy level. Thus, when acetone adsorbs on the ZnSnO$_3$(001) surface in M5, the bonding between the O in the methyl acetate product and the O atom on the surface is mainly associated with the O-p orbital. Figure 10c shows that the C atom in the carbonyl group and O atom in the O$_2^-$ undergo strong hybridization, where the peak overlap of the p orbitals is near the Fermi level and the s-orbital overlap is at a low energy level. The PDOS analysis shows a newly formed and stable C-O bond in M5 [48].

The DFT results show that two main reaction paths can cause changes in material resistance. The first reaction path consists of acetone replacing the pre-adsorbed O$_2^-$ and directly adsorbing on Sn^{4+} on the surface through ionic bonds. The second path is that acetone reacts with the surface to generate an acetone-O complex. Compared with the first reaction path, this reaction process is accompanied by a large amount of charge transfer, which can significantly change the resistance of the ZnSnO$_3$(001) surface results in improving gas sensitivity. However, the second reaction path cannot proceed spontaneously at room temperature, and the E_{ads} at high temperatures is much smaller than that of the first reaction path. This result is caused by the dissociation of pre-adsorbed O$_2^-$ and the cleavage of the Sn–O bond. Therefore, under normal temperature conditions, acetone molecules can only react with the surface of ZnSnO$_3$ through the first reaction path, while at high temperatures, acetone molecules can react with the surface of ZnSnO$_3$ through two reaction paths. This
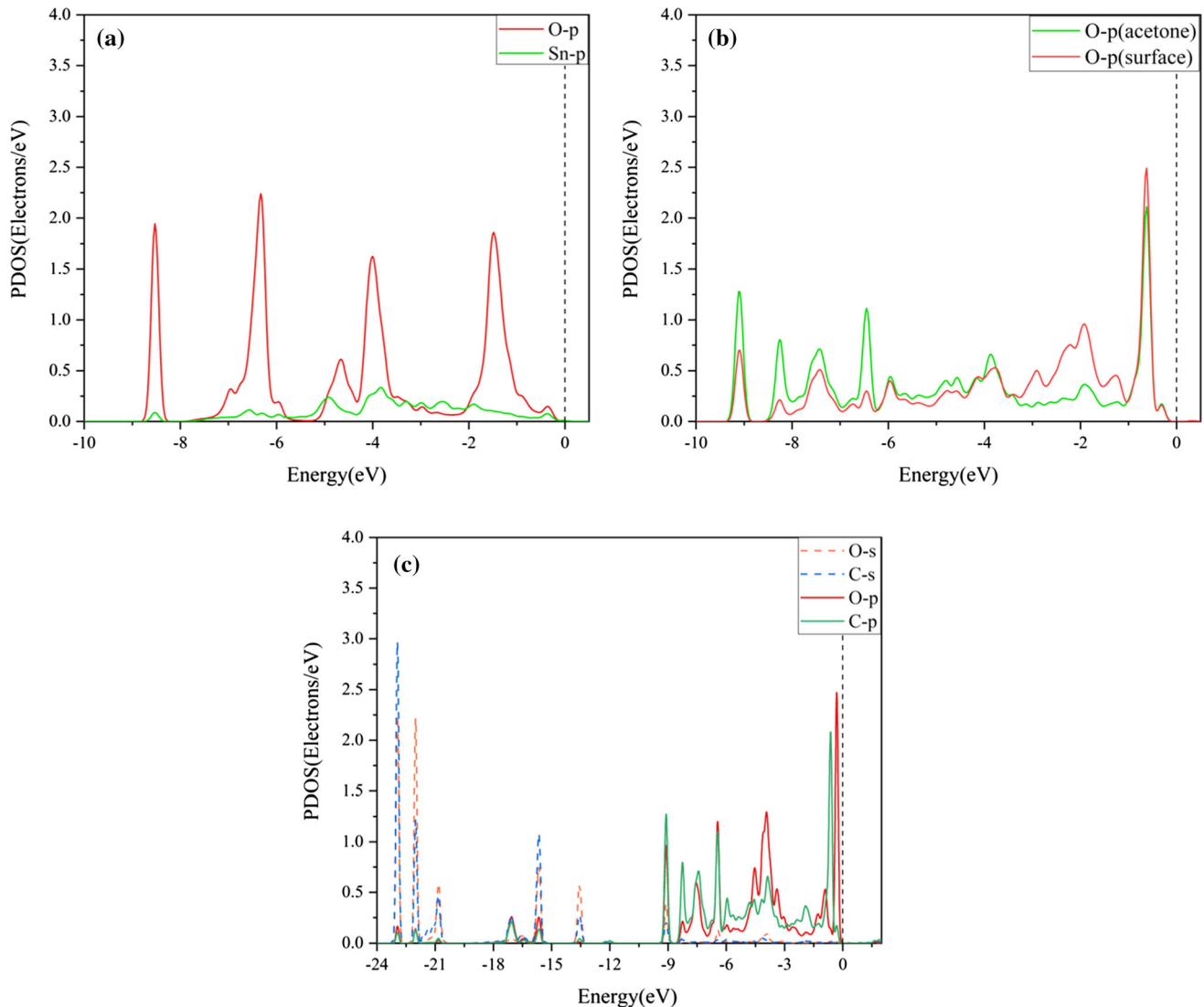
Figure 10 The PDOS of M4 and M5. **a** The PDOS of O atoms of acetone and Sn ion in M4; **b** The PDOS of O atoms of acetone and O atoms of surface in M5; **c** The PDOS of C atom in the carbonyl group and O atom from pre-adsorbed O_2.

result shows that $ZnSnO_3$ nanosheets can exhibit higher sensitivity at high temperatures.

Interaction between $ZnSnO_3(001)$ surface with pre-adsorbed O^- and acetone gas

An adsorption model of acetone molecules on the $ZnSnO_3(001)$ surface with pre-adsorbed O^- after O_2^- decomposed into O^- at high temperatures was analyzed to elucidate the gas-sensing mechanism via adsorption at high temperatures. The results presented above show that the Sn site on the $ZnSnO_3(001)$ surface is the active adsorption site. Therefore, the $ZnSnO_3(001)$ surface with an O atom adsorbed at the Sn site was selected as the pre-

adsorbed surface, and acetone molecules were introduced to the model with the pre-adsorbed surface. Figure 11 shows the four initial adsorption models that were first considered. Structural optimization produced acetone molecules being close to the surface for models K1-K3, whereas the acetone molecules are far away from the surface for model K4. Thus, proximity of the H end of the acetone molecule to the surface precludes adsorption. Since the dissociation reaction of oxygen molecules only occurs at high temperatures, in this section the E_{ads} is only corrected at 623.15 K, 1 atm. As shown in Table 4, the E_{ads} of K1, K2 and K3 are all less than zero, indicating the spontaneous interaction between acetone molecules and the $ZnSnO_3(001)$ surface with

Figure 11 The configuration of molecular acetone adsorption on ZnSnO$_3$ (001) surface of pre-adsorbed O$^-$. The left are before optimizing the structure. The right are after optimizing the structure. (K1) Acetone is above the pre-adsorbed oxygen and the carbon atoms is close to the pre-adsorbed O; (K2) Acetone is above the pre-adsorbed oxygen and the O end is close to the pre-adsorbed O; (K3) Acetone is above the surface and O end are close to the surface; (K4) Acetone is above the surface and H end are close to the surface.
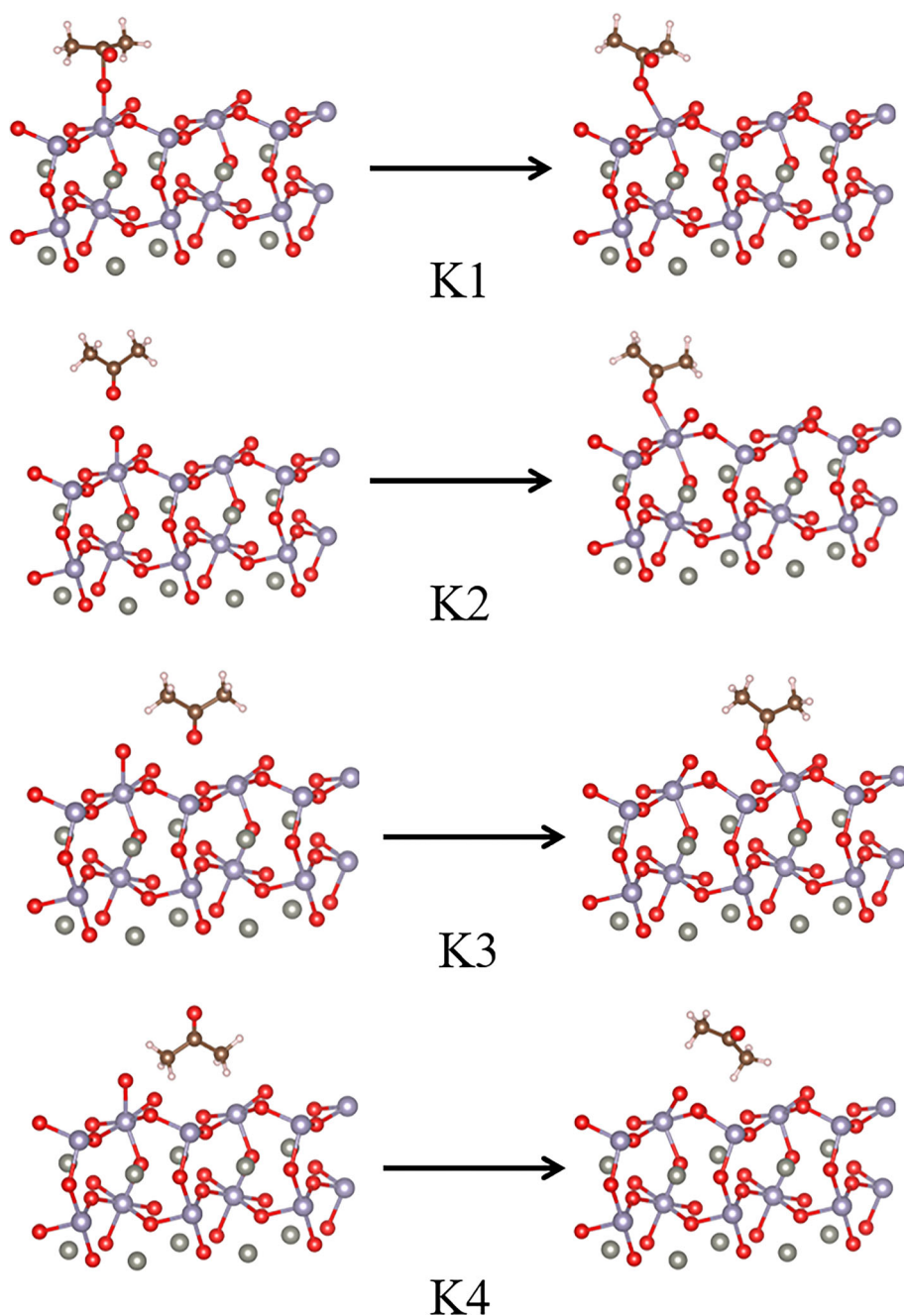

Table 4 Properties of the adsorption acetone molecular on the ZnSnO$_3$(001) surface of pre-adsorbed O$^-$

Model	E_{ads} (eV)	Charge transfer of C$_3$H$_6$O (e)
K1	− 1.16	− 0.59
K2	− 1.65	− 0.10
K3	− 1.63	− 0.11

pre-adsorbed O$^-$. The Bader charge analysis shows that the acetone molecules in K1, K2, and K3

lose − 0.59 e, − 0.10 e, and − 0.11 e electrons, respectively, demonstrating that the acetone molecules donate electrons to the surface during the adsorption reaction.

DOS and CDD analyses were carried out to elucidate the gas-sensing mechanism of the ZnSnO$_3$(001) surface with pre-adsorbed O$^-$. Comparing the DOS plot of free acetone with those presented in Fig. 12 for acetone adsorption with the three optimized models shows a shift to the low energy side for all three

models and a significant change in the peak structure. Thus, chemical adsorption occurs between the acetone and the surface for the three models. As the DOS plots of acetone molecules are similar for K2 and K3, the adsorption reactions for K2 and K3 are also similar. Therefore, K1 and K2 were selected as representative models for PDOS and CDD analyses. Figure 13 shows the PDOS analysis of K1 and K2. Figure 13a shows that in K1, the p orbital of the C atom in the carbonyl group of the acetone molecule overlaps the p orbital of the pre-adsorbed O, demonstrating the formation of a new C-O bond. Figure 13b shows strong orbital hybridization in K2 between the O-p orbital in acetone and the Sn-p orbital on the surface. The CDD plots of K1 and K2 (Fig. 14) show that the pre-adsorbed O^- ion first attacks the positively charged C center in the carbonyl group of acetone molecule to form methyl acetate and is then adsorbed to the Sn site on the surface via the pre-adsorbed O^- (Fig. 14a). In K2, the negatively charged O center in the carbonyl group of acetone molecule first undergoes a nucleophilic reaction with Sn^{4+} on the surface and then adsorbs on the surface. This adsorption process is very similar to that for M4 (Fig. 14b).

The DFT calculation results show that there are two reaction paths with high charge transfer between the acetone molecules and the $ZnSnO_3$ nanosheets. The first path is the direct adsorption of acetone molecules on Sn^{4+} on the surface, and the second path is the chemical reaction of acetone with the pre-
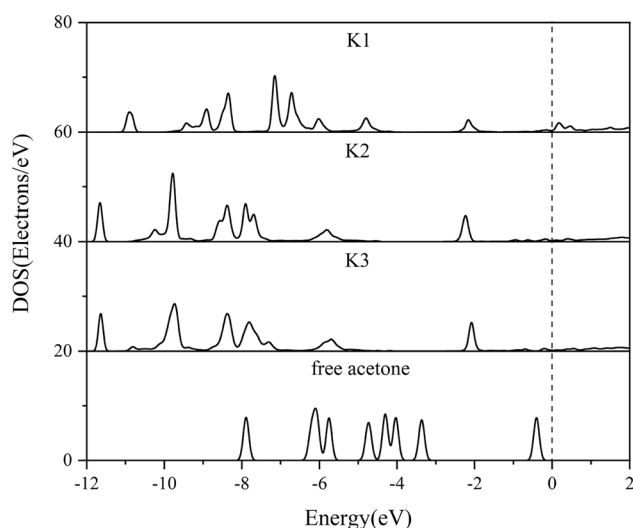
adsorbed O^-, followed by forming acetone-O complex adsorption on the surface via the pre-adsorbed O^-. In the second adsorption reaction path, the amount of charge transfer increases significantly, which played a critical role in the response of the $ZnSnO_3$ to the acetone gas.

Experimental result

Synthesis and characterization of ZnSnO₃

Figure 15 shows the characterization results of the synthesized $ZnSnO_3$. The crystalline phases of prepared $ZnSnO_3$ were characterized by XRD in Fig. 15a, the peaks can be classified as perovskite orthorhombic $ZnSnO_3$(JCPDS 28-1486), indicating the successful preparation of perovskite-type $ZnSnO_3$[49]. The crystal size of $ZnSnO_3$ nanosheets is calculated by the Scherrer formula, as shown in Eq. (8),

$$D = (0.89 * \lambda)/(\beta * \cos\theta) \tag{8}$$

where D is the crystal size, λ is the wavelength of incident X-ray, β is the half-width of the diffraction peak, and θ is the diffraction angle. After calculation, the crystal size of $ZnSnO_3$ nanosheets is about 17 nm.

The SEM images of the $ZnSnO_3$ nanosheet are shown in Fig. 16. As shown in Fig. 16a, the low-magnification SEM images demonstrate that the synthesized $ZnSnO_3$ is a sheet-like structure with holes on the surface of the sheet. This phenomenon can be significantly observed in the high magnification SEM images (Fig. 16b). After measurement, the surface hole diameters of the $ZnSnO_3$ nanosheets are about 10–40 nm. To further confirm the morphologies and structures of the $ZnSnO_3$ nanosheet, TEM was performed. As shown in Fig. 17a, the side length of the $ZnSnO_3$ nanosheet is between 80 and 200 nm and the size distribution is relatively uniform. In addition, as shown in Fig. 17c, the structure of the hole on the surface could be observed, the diameter is about 19.7 nm, which identifies with the results of SEM. In the HRTEM image (Fig. 17b), a well-resolved lattice fringe of 0.26 nm and 0.33 nm can be observed, which corresponds to the (110) and (012) crystal face of $ZnSnO_3$, respectively. As shown in Figs. 17d–f, according to the EDX results, the uniform distribution of Sn, Zn, O elements confirms that $ZnSnO_3$ nanosheet was successfully obtained. The element atomic fraction percentage of Zn, Sn, O in the nanosheet is calculated as 20.15%, 21.85%, 57.9%,
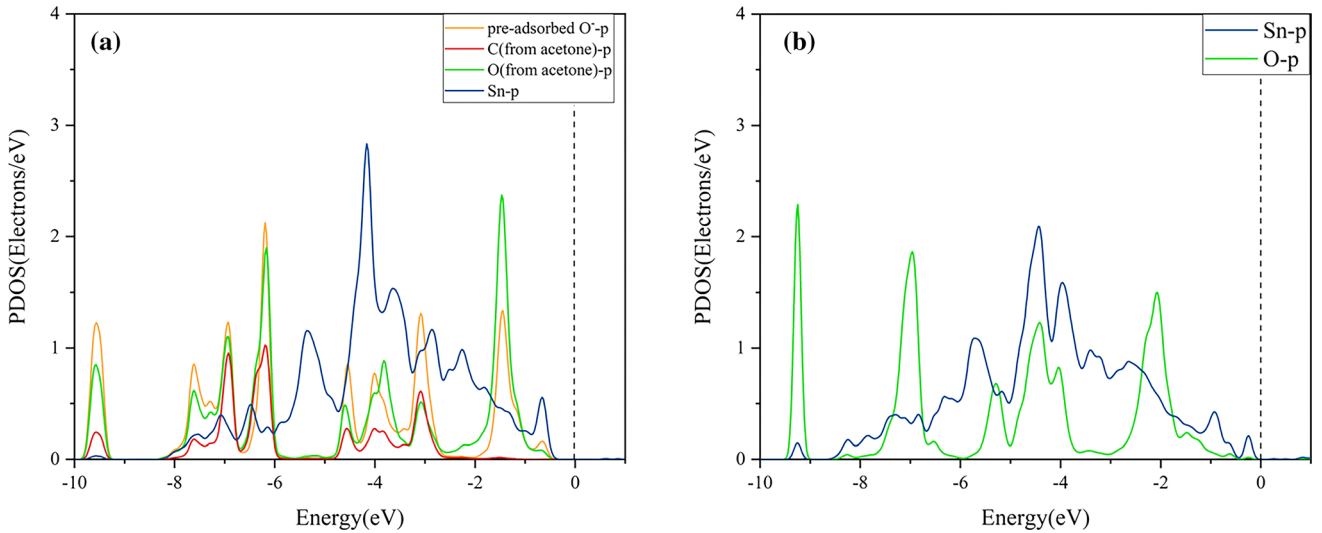

Figure 12 The DOS of free acetone and adsorbed acetone in K1-K3.

Figure 13 The PDOS of model K1 and K2, **a** The POS of pre-adsorbed O⁻ and C of acetone; **b** The POS of O atom of acetone and Sn atom.
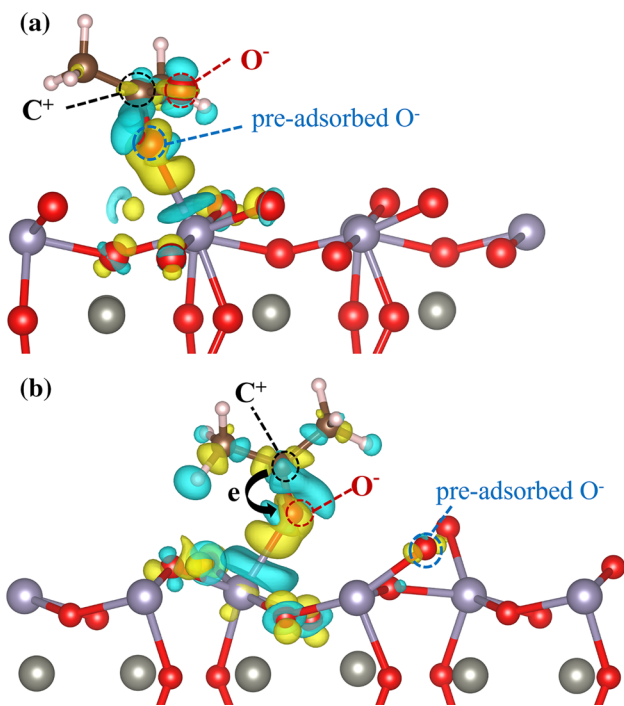

Figure 14 The CDD of model M1 and M2, blue represents the region of charge divergence, yellow represents the region of charge convergence, **a** model M1; **b** model M2. The isosurfaces refer to isovalues of 1×10^{-3} electrons/bohr³.

respectively. The atomic ratio of Zn: Sn: O was close to 1: 1: 3, further proving that $ZnSnO_3$ nanosheet was successfully prepared.
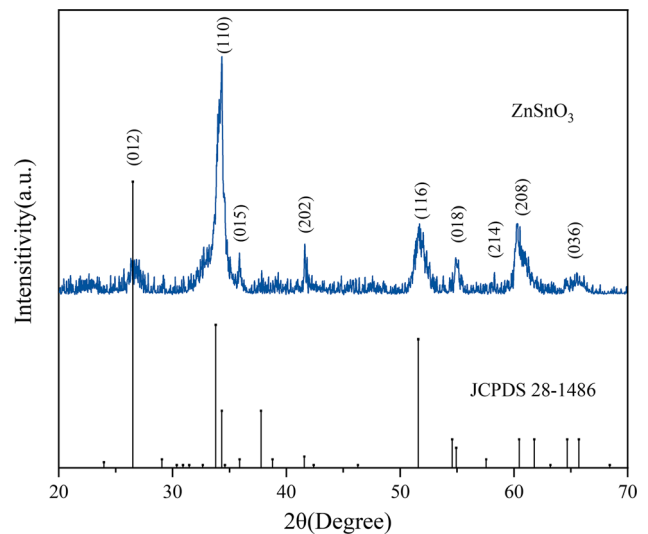

Figure 15 The XRD of the $ZnSnO_3$ nanosheet.

Gas sensitivity test

Figure 18 shows the gas sensitivity test results of sheet-like $ZnSnO_3$, including the optimal operating temperature, concentration analysis, and selectivity measurement. The sensitivity of the $ZnSnO_3$ sensor to acetone gradually increased with the temperature, reaching 125.444 at 350 °C (Fig. 18a). The sensitivity trended downward upon increasing the temperature further, indicating 350 °C as the optimal operating temperature. According to the previous DFT calculation results, the chemical reaction between the
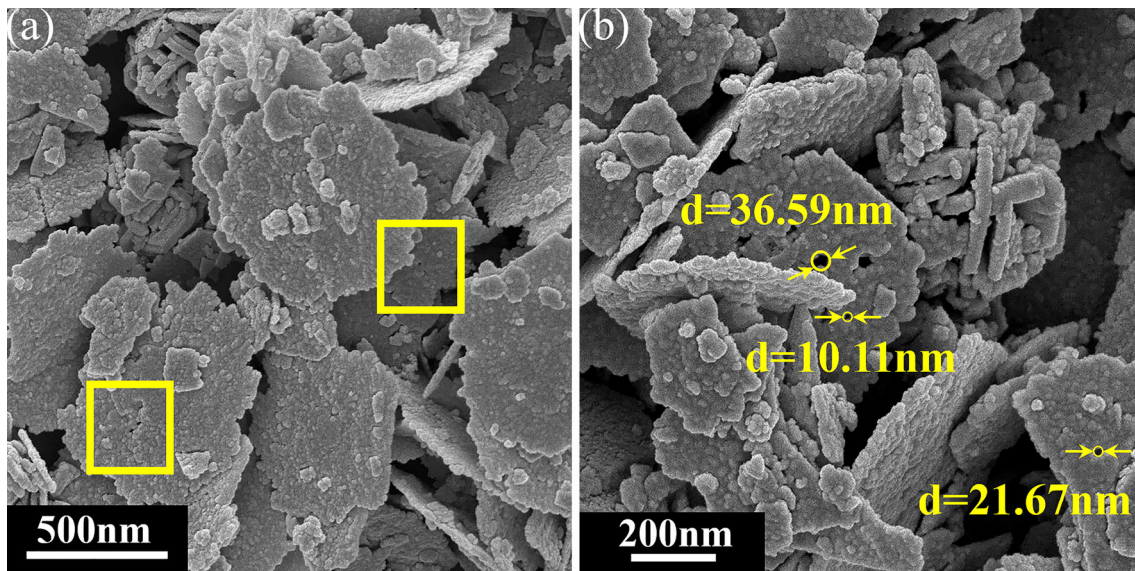
**Figure 16** The **a** low magnification; **b** high magnification SEM images of the ZnSnO₃ nanosheet.

acetone molecule and the surface of the material is divided into low charge transfer reaction and high charge transfer reaction. The low charge transfer reaction is more likely to occur, but it is hard to cause a significant change in the resistance of the material. The high charge transfer reaction is accompanied by a large amount of charge transfer in the process, which can cause significant changes in the resistance of the material, but it is not easy to occur because of the high energy barrier that compares with low charges transfer reaction. Therefore additional energy supply can break the energy barrier and promote the occurrence of high charge transfer reactions. Before the operating temperature of the $ZnSnO_3$ sensor up to the optimal temperature, the increase of the operating temperature makes the high charges transfer reaction occur easily, resulting in the continuous improvement of sensitivity for $ZnSnO_3$. However, the desorption rate was higher than the adsorption rate above the optimal working temperature, resulting in a decrease in the sensitivity [50].

A concentration–response test is an important means of measuring the responsivity of gas-sensitive materials. The sensitivity of the $ZnSnO_3$ sensor gradually increased with the acetone concentration, where the sensitivities to 5–500 ppm acetone were 8.37, 23.745, 81.398, 106.167, 122.252, 194.953, 222.567, and 390.636 (Fig. 18b). In practice, a sensor should not be affected by a complex environment containing multiple gases with similar properties, while being

selective to the target gas. The test results presented that in Fig. 18c, the sensitivity of $ZnSnO_3$ sensor to 100 ppm of five VOCs of ammonia, methanol, mathanal, ethanol, and acetone at 350 °C was 14.676, 55.48, 43.257, 33.304, and 125.444, respectively. The $ZnSnO_3$ sensor was 7.39, 2.26, 2.89, or 3.73 times more sensitive to acetone than the other VOCs. It is evident that the sensor exhibits good selectivity to acetone gas and could accurately detect acetone in a complex gas environment. In addition, Fig. 18c also shows the dynamic resistance curve of sheet-like $ZnSnO_3$. The resistance of the material decreases in an acetone atmosphere and increases in an acetone-free environment. This phenomenon is consistent with the sensing behavior of n-type semiconductors for reducing gases.

As shown in Fig. 18d, when the $ZnSnO_3$ sensor in the acetone atmosphere, reacts with acetone gas quickly and the resistance value decreases rapidly. This phenomenon fits well with the DFT results during the chemical reaction $ZnSnO_3$ gains electrons, thus the carrier concentration increases resulting in the resistance decreases between the $ZnSnO_3$ and acetone gas. The response/recovery time of $ZnSnO_3$ was 4 s/27 s (Fig. 18e), this is due to the sheet structure and the micro-holes on the surface of the material providing a large specific surface area and more active sites, which is conducive to the rapid reaction between the target molecule and the surface of material. To further evaluate the long-term

Figure 17 The **a** TME image; **b** HRTEM images; **c**–**f** EDX images of the ZnSnO₃ nanosheet.
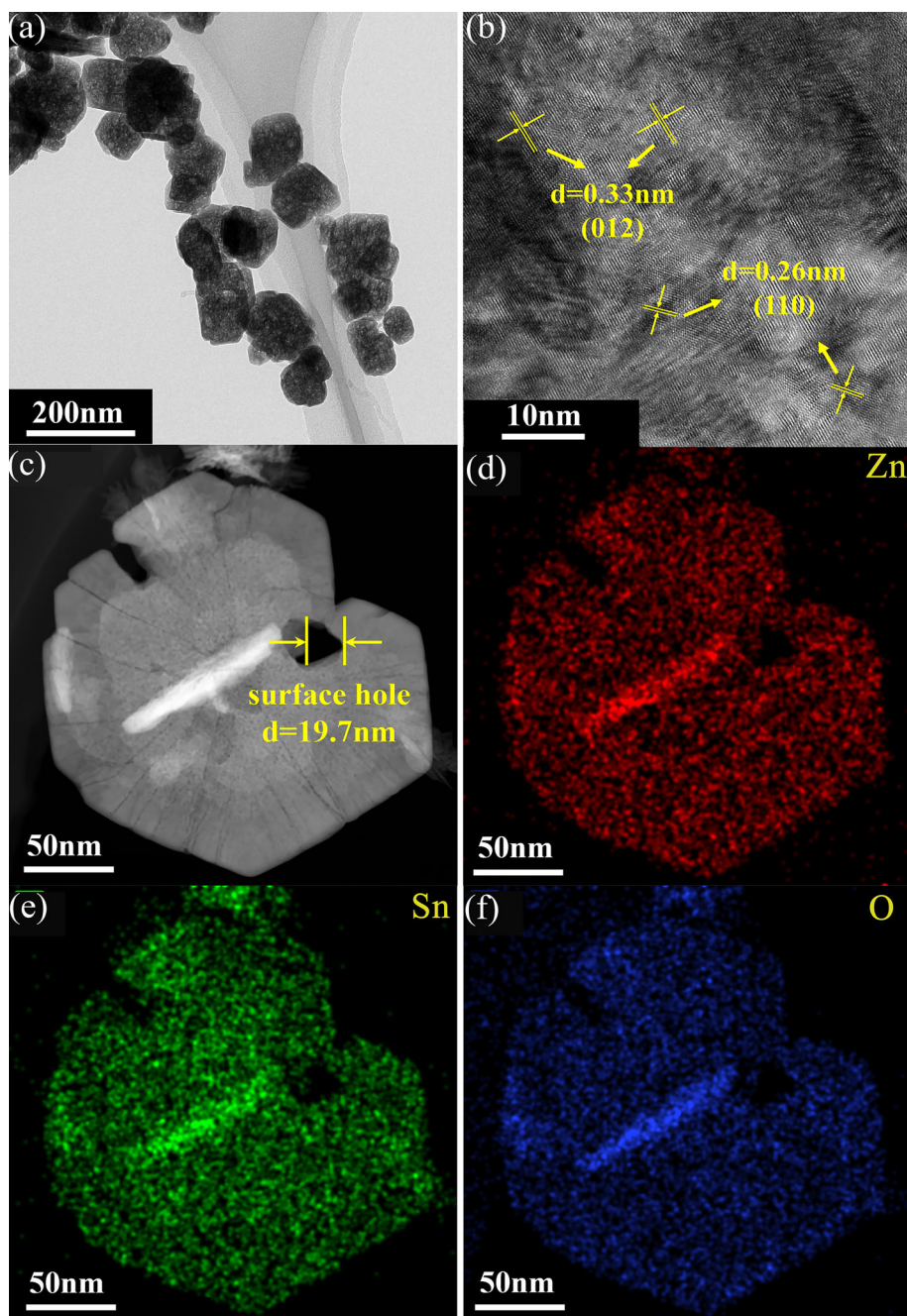
stability and repeatability of the sensor, the sensitivity of sheet-like ZnSnO₃ sensor to 10/100 ppm acetone was tested. The test period was 35 days, and five tests were performed at an interval of seven days. As shown in the Fig. 18f, the sensitivities to 10/100 ppm acetone were 22.074, 21.665, 23.674, 20.563, 19.788 and 129.535, 129.745, 124.863, 122.804, 122.729, respectively. The sensitivity showed a slightly decreasing trend, but the result indicated that the sheet-like ZnSnO₃ sensor has excellent stability and repeatability to 10 ppm/100 ppm acetone. The sensitivity of the fifth test still reached 89.64% and 94.74%, respectively, of that of the first test, indicating that the sheet-like ZnSnO₃ sensor had a good application potential in practical applications.

Compared with other sensors for 100 ppm acetone summarized in Table 5, the sheet-like ZnSnO₃ presents the highest sensitivity and excellent response/recovery time, the sensitivity even higher than other sensors which at 250 ppm. However, the ZnSnO₃
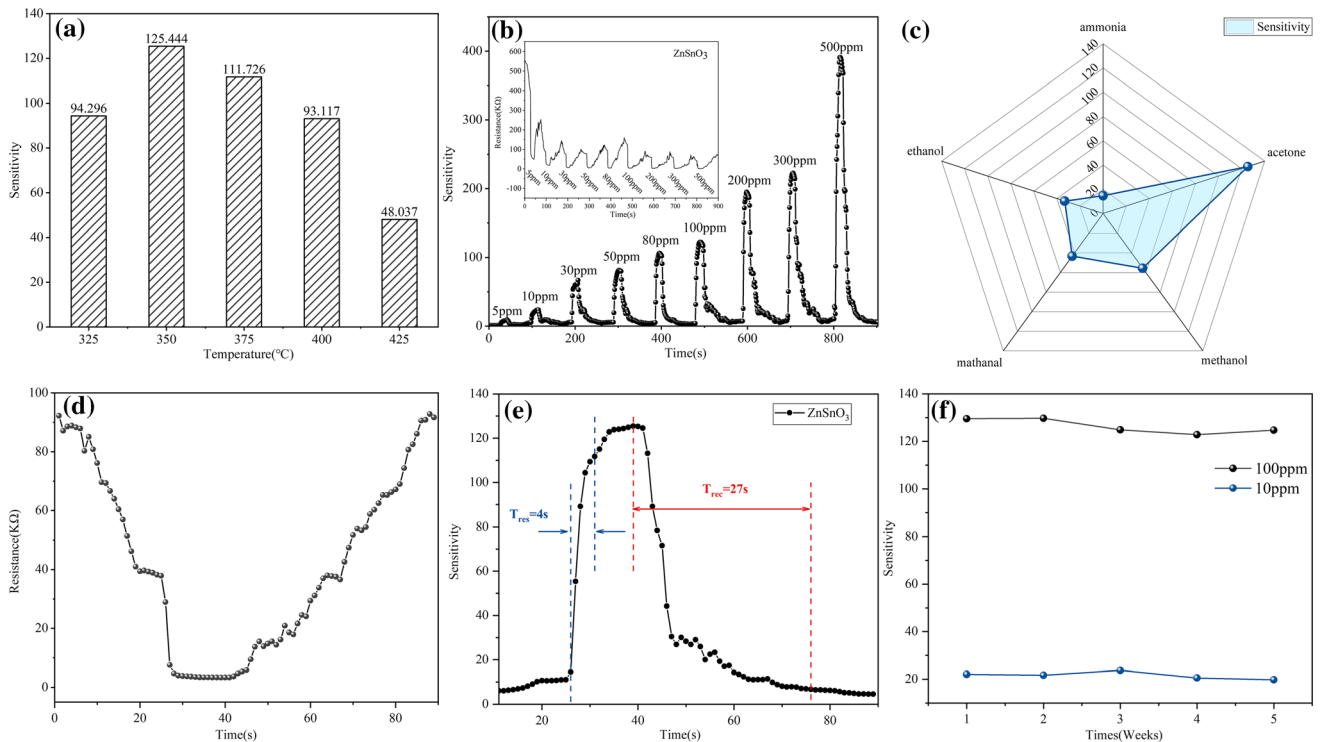
Figure 18 Test results for gas sensitivity; **a** The working temperature and sensitivity curves of sheet-like ZnSnO₃ materials in 100 ppm acetone gas; **b** The response curve of the sheet-like ZnSnO₃ sensor to acetone gas at concentrations of 5–500 ppm at 350 °C (insert: The Dynamic resistance curve); **c** The response curve of the sheet-like ZnSnO₃ sensor to 50 ppm acetone gas at 425 °C; **d** Resistance change curves of sheet-like ZnSnO₃ sensor; **e** The response/recovery time curve of sheet-like ZnSnO₃ sensor to acetone. (350 °C, 100 ppm); **f** The repeatability and stability test of ZnSnO₃ sheet-like sensor to 10 ppm/100 ppm acetone gas at 350 °C.

Table 5 The performance comparison between ZnSnO₃ sensor and acetone gas sensor reported previously

Material	Operating temperature (°C)	Gas concentration (ppm)	Response/Recovery time(s)	Sensitivity	Reference
Fe_2O_3 foam	300	100	4/10	11.6	[51]
In_2O_3/MWCNT	300	250	9/96	15.97	[52]
ZnO/NiO	275	100	1/20	29.8	[53]
Co_3O_4	180	100	43/96	7.6	[54]
ZnO	400	100	6/5	20.27	[55]
$ZnSnO_3$	350	100	4/27	125.44	This paper

sensor has a higher optimal operating temperature. Therefore, reducing the optimal working temperature and further improving the sensitivity is the focal point direction in the follow-up subject.

Conclusions

A detailed study of the adsorption of acetone gas by ZnSnO₃ was carried out using calculations and experiments. According to the DFT calculation results, there is a strong interaction between the surface of ZnSnO₃(001) pre-adsorbed O^- and O_2^- and acetone molecules. During the adsorption reaction, electrons are transferred from acetone to the surface. The adsorption reaction can be divided into low charge transfer reaction and high charge transfer reaction. Compared with low charge transfer reaction, high charge transfer reaction always has the generation of acetone-O complex, in addition, the reaction process due to a large amount of charge transfer, the resistance of the material can be

significantly changed to improve the sensitivity of the ZnSnO$_3$ sensor, but it has a higher energy barrier thus it is difficult to occur. The prepared perovskite-type ZnSnO$_3$ has a sheet-like structure with a side length of approximately 80–200 nm, resulting in a large specific surface area that provides a large number of active adsorption sites. Gas sensitivity test results showed that the sensitivity of the ZnSnO$_3$ increases with the increase in operating temperature, until the optimal operating temperature of 350 °C, this is because the increase in temperature is conducive to the occurrence of high charge transfer reactions. The sensitivity of ZnSnO$_3$ to 5 ppm acetone was 8.37. A selectivity test showed that ZnSnO$_3$ was more than two times more selectivity to acetone than five other VOCs and 7.39 times more selectivity to acetone than ammonia gas. In the five-week stability and repeatability test, the sensitivity to 10/100 ppm acetone of sheet-like ZnSnO$_3$ sensor could still maintain at 89.64% and 94.74% of the first test result. The study results show that ZnSnO$_3$ can accurately detect acetone gas with excellent selectivity. This study provides theoretical guidance for future research and development of a ZnSnO$_3$ sensor.

Acknowledgements

Declarations

Conflict of interest The authors declare that there are no competing interests regarding the publication of this paper.

References

[1] Mo Y, Li H, Zhou K et al (2019) Acetone adsorption to (BeO)$_{12}$, (MgO)$_{12}$ and (ZnO)$_{12}$ nanoparticles and their graphene composites: a density functional theory (DFT) study. Appl Surf Sci 469:962. https://doi.org/10.1016/j.apsusc.2018.11.079

[2] Wang CC, Weng YC, Chou TC (2007) Acetone sensor using lead foil as working electrode. Sens Actuators B Chem 122:591. https://doi.org/10.1016/j.snb.2006.07.003

[3] Liu F, Chu X, Dong Y, Zhang W, Sun W, Shen L (2013) Acetone gas sensors based on graphene-ZnFe$_2$O$_4$ composite prepared by solvothermal method. Sens Actuators B Chem 188:469. https://doi.org/10.1016/j.snb.2013.06.065

[4] Patil SB, Patil PP, More MA (2007) Acetone vapour sensing characteristics of cobalt-doped SnO$_2$ thin films. Sens Actuators B Chem 125:126. https://doi.org/10.1016/j.snb.2007.01.047

[5] Mehaney A, Ahmed AM (2020) Theoretical design of porous phononic crystal sensor for detecting CO$_2$ pollutions in air. Phys E Low Dimens Syst Nanostruct. https://doi.org/10.1016/j.physe.2020.114353

[6] Ahmed AM, Mehaney A (2019) Ultra-high sensitive 1D porous silicon photonic crystal sensor based on the coupling of Tamm/Fano resonances in the mid-infrared region. Sci Rep 9:6973. https://doi.org/10.1038/s41598-019-43440-y

[7] Dai J, Ogbeide O, Macadam N et al (2020) Printed gas sensors. Chem Soc Rev 49:1756. https://doi.org/10.1039/c9cs00459a

[8] Zhao J, Huo LH, Gao S, Zhao H, Zhao JG (2006) Alcohols and acetone sensing properties of SnO$_2$ thin films deposited by dip-coating. Sens Actuators B Chem 115:460. https://doi.org/10.1016/j.snb.2005.10.024

[9] Kim DH, Jang JS, Koo WT, Choi SJ, Kim SJ, Kim ID (2018) Hierarchically interconnected porosity control of catalyst-loaded WO$_3$ nanofiber scaffold: superior acetone sensing layers for exhaled breath analysis. Sens Actuators B Chem 259:616. https://doi.org/10.1016/j.snb.2017.12.051

[10] Nakate UT, Ahmad R, Patil P, Yu YT, Hahn YB (2020) Ultra thin NiO nanosheets for high performance hydrogen gas sensor device. Appl Surf Sci. https://doi.org/10.1016/j.apsusc.2019.144971

[11] Jin X, Li Y, Zhang B, Xu X, Sun G, Wang Y (2021) Temperature-dependent dual selectivity of hierarchical porous In$_2$O$_3$ nanospheres for sensing ethanol and TEA. Sens Actuators B Chem. https://doi.org/10.1016/j.snb.2020.129271

[12] Tanvir NB, Yurchenko O, Laubender E, Urban G (2017) Investigation of low temperature effects on work function based CO$_2$ gas sensing of nanoparticulate CuO films. Sens Actuators B Chem 247:968. https://doi.org/10.1016/j.snb.2016.11.020

[13] Chen Y, Qin H, Wang X, Li L, Hu J (2016) Acetone sensing properties and mechanism of nano-LaFeO$_3$ thick-films. Sens

Actuators B Chem 235:56. https://doi.org/10.1016/j.snb.2016.05.059

[14] Peng Y, Si W, Li J, Crittenden J, Hao J (2015) Experimental and DFT studies on Sr-doped LaMnO$_3$ catalysts for NO$_x$ storage and reduction. Catal Sci Technol 5:2478. https://doi.org/10.1039/c5cy00073d

[15] Han T, Ma S, Yun P et al (2021) Synthesis and characterization of Ho-doped SmFeO$_3$ nanofibers with enhanced glycol sensing properties. Vacuum. https://doi.org/10.1016/j.vacuum.2021.110378

[16] Wang Z, Miao J, Zhang H, Wang D, Sun J (2020) Hollow cubic ZnSnO$_3$ with abundant oxygen vacancies for H$_2$S gas sensing. J Hazard Mater 391:122226. https://doi.org/10.1016/j.jhazmat.2020.122226

[17] Guo H, Chen H, Zhang H et al (2019) Low-temperature processed yttrium-doped SrSnO$_3$ perovskite electron transport layer for planar heterojunction perovskite solar cells with high efficiency. Nano Energy 59:1. https://doi.org/10.1016/j.nanoen.2019.01.059

[18] Biausque G, Schuurman Y (2010) The reaction mechanism of the high temperature ammonia oxidation to nitric oxide over LaCoO$_3$. J Catal 276:306. https://doi.org/10.1016/j.jcat.2010.09.022

[19] Lee YL, Kleis J, Rossmeisl J, Morgan D (2009) Ab initioenergetics of LaBO$_3$ (001) (B=Mn, Fe Co, and Ni) for solid oxide fuel cell cathodes. Phys Rev B. https://doi.org/10.1103/PhysRevB.80.224101

[20] Jonathan H, Reshma RR, Livia G, Yu K, Yang Y, Yang SH (2017) Perovskites in catalysis and electrocatalysis. Science 358:751

[21] Zhou Y, Lü Z, Li J, Xu S, Xu D, Wei B (2021) The electronic properties and structural stability of LaFeO$_3$ oxide by niobium doping: a density functional theory study. Int J Hydrog Energy 46:9193. https://doi.org/10.1016/j.ijhydene.2020.12.202

[22] Li X, Zhao H, Xu N, Zhou X, Zhang C, Chen N (2009) Electrical conduction behavior of La, Co co-doped SrTiO$_3$ perovskite as anode material for solid oxide fuel cells. Int J Hydrog Energy 34:6407. https://doi.org/10.1016/j.ijhydene.2009.05.079

[23] Shaban M, Rabia M, Eldakrory MG, Maree RM, Ahmed AM (2020) Efficient photoselectrochemical hydrogen production utilizing of APbI$_3$ (A = Na, Cs, and Li) perovskites nanorods. Int J Energy Res 45:7436. https://doi.org/10.1002/er.6326

[24] Balamurugan C, Song SJ, Lee DW (2018) Porous nanostructured GdFeO$_3$ perovskite oxides and their gas response performance to NO$_x$. Sens Actuators B Chem 272:400. https://doi.org/10.1016/j.snb.2018.05.125

[25] Ghasdi M, Alamdari H (2010) CO sensitive nanocrystalline LaCoO$_3$ perovskite sensor prepared by high energy ball milling. Sens Actuators B Chem 148:478. https://doi.org/10.1016/j.snb.2010.05.056

[26] Chaudhari GN, Jagtap SV, Gedam NN, Pawar MJ, Sangawar VS (2009) Sol-gel synthesized semiconducting LaCo$_{0.8}$Fe$_{0.2}$O$_3$-based powder for thick film NH$_3$ gas sensor. Talanta 78:1136. https://doi.org/10.1016/j.talanta.2009.01.030

[27] Chen Y, Qin H, Shi C, Li L, Hu J (2015) High temperature CO$_2$ sensing properties and mechanism of nanocrystalline LaCrO$_3$ with rhombohedral structure: experiments and ab initio calculations. RSC Adv 5:54710. https://doi.org/10.1039/c5ra05081b

[28] Xie C, Zhu B, Sun Y, Song W, Xu M (2021) Effect of doping Cr on NH$_3$ adsorption and NO oxidation over the Fe$_x$O$_y$/AC surface: a DFT-D study. J Hazard Mater 416:125798. https://doi.org/10.1016/j.jhazmat.2021.125798

[29] Li X, Gao H (2020) Influence of Ce doping on catalytic oxidation of NO on LaCoO$_3$ (011) surface: a DFT study. Appl Surf Sci. https://doi.org/10.1016/j.apsusc.2019.143866

[30] Wu M, Chen S, Xiang W (2020) Oxygen vacancy induced performance enhancement of toluene catalytic oxidation using LaFeO$_3$ perovskite oxides. Chem Eng J. https://doi.org/10.1016/j.cej.2020.124101

[31] Choi KH, Siddiqui GU, Yang B-s, Mustafa M (2015) Synthesis of ZnSnO$_3$ nanocubes and thin film fabrication of (ZnSnO$_3$/PMMA) composite through electrospray deposition. J Mater Sci Mater Electron 26:5690. https://doi.org/10.1007/s10854-015-3121-1

[32] Gou H, Gao F, Zhang J (2010) Structural identification, electronic and optical properties of ZnSnO$_3$: first principle calculations. Comput Mater Sci 49:552. https://doi.org/10.1016/j.commatsci.2010.05.049

[33] Honer CJ, Prosniewski MJ, Putatunda A, Singh DJ (2017) Properties of the antiferromagnetic selenite MnSeO$_3$ and its non-magnetic analogue ZnSnO$_3$ from first principles calculations. J Phys Condens Matter 29:405501. https://doi.org/10.1088/1361-648X/aa7f89

[34] Xu J, Jia X, Lou X, Shen J (2006) One-step hydrothermal synthesis and gas sensing property of ZnSnO$_3$ microparticles. Solid-State Electron 50:504. https://doi.org/10.1016/j.sse.2006.02.001

[35] Guo W, Liu T, Yu W, Huang L, Chen Y, Wang Z (2013) Rapid selective detection of formaldehyde by hollow ZnSnO$_3$ nanocages. Phys E Low Dimens Syst Nanostruct 48:46. https://doi.org/10.1016/j.physe.2012.11.021

[36] Wadkar P, Bauskar D, Patil P (2013) High performance H$_2$ sensor based on ZnSnO$_3$ cubic crystallites synthesized by a hydrothermal method. Talanta 105:327. https://doi.org/10.1016/j.talanta.2012.10.051

[37] Kresse G, Furthmüller J (1996) Efficient iterative schemes for ab initio total-energy calculations using a plane-wave basis set. Phys Rev B 54:11169

[38] Blochl PE (1994) Projector augmented-wave method. Phys Rev B Condens Matter 50:17953. https://doi.org/10.1103/physrevb.50.17953

[39] Perdew JP, Burke K, Ernzerhof M (1996) Generalized gradient approximation made simple. Phys Rev Lett 77:3865

[40] Grimme S (2006) Semiempirical GGA-type density functional constructed with a long-range dispersion correction. J Comput Chem 27:1787. https://doi.org/10.1002/jcc.20495

[41] Grimme S, Antony J, Ehrlich S, Krieg H (2010) A consistent and accurate ab initio parametrization of density functional dispersion correction (DFT-D) for the 94 elements H-Pu. J Chem Phys 132:154104. https://doi.org/10.1063/1.3382344

[42] Wang V, Xu N, Liu JC, Tang G, Geng WT, (2019) VASP-KIT: A User-Friendly Interface Facilitating High-throughput Computing and Analysis Using VASP Code. http://arxiv.org/abs/arXiv:1908.08269

[43] Habibi MH, Mardani M (2017) Synthesis and characterization of bi-component ZnSnO$_3$/Zn$_2$SnO$_4$ (perovskite/spinel) nano-composites for photocatalytic degradation of Intracron Blue: Structural, opto-electronic and morphology study. J Mol Liq 238:397. https://doi.org/10.1016/j.molliq.2017.05.011

[44] Sadeghian Lemraski M, Nadimi E (2017) Acetone gas sensing mechanism on zinc oxide surfaces: a first principles calculation. Surf Sci 657:96. https://doi.org/10.1016/j.susc.2016.11.013

[45] Liu X, Hu J, Cheng B, Qin H, Zhao M, Yang C (2009) First-principles study of O$_2$ adsorption on the LaFeO$_3$ (010) surface. Sens Actuators B Chem 139:520. https://doi.org/10.1016/j.snb.2009.03.052

[46] Chen X, Tan C, Yang Q et al (2016) Ab initio study of the adsorption of small molecules on stanene. J Phys Chem C 120:13987. https://doi.org/10.1021/acs.jpcc.6b04481

[47] Singh-Miller NE, Marzari N (2009) Surface energies, work functions, and surface relaxations of low-index metallic surfaces from first principles. Phys Rev B. https://doi.org/10.1103/PhysRevB.80.235407

[48] Sun L, Li G, Chen W, Luo F, Hu J, Qin H (2014) Adsorption of CO on the LaCoO$_3$ (001) surface by density functional theory calculation. Appl Surf Sci 309:128. https://doi.org/10.1016/j.apsusc.2014.04.202

[49] Dong S, Xia L, Chen X et al (2021) Interfacial and electronic band structure optimization for the adsorption and visible-light photocatalytic activity of macroscopic ZnSnO$_3$/-graphene aerogel. Compos B Eng. https://doi.org/10.1016/j.compositesb.2021.108765

[50] Sharma A, Tomar M, Gupta V (2013) A low temperature operated NO$_2$ gas sensor based on TeO$_2$/SnO$_2$ p–n heterointerface. Sens Actuators B Chem 176:875. https://doi.org/10.1016/j.snb.2012.09.029

[51] Han D, Zhao M (2020) Facile and simple synthesis of novel iron oxide foam and used as acetone gas sensor with sub-ppm level. J Alloys Compd. https://doi.org/10.1016/j.jallcom.2019.152406

[52] Kohli N, Hastir A, Kumari M, Singh RC (2020) Hydrothermally synthesized heterostructures of In$_2$O$_3$/MWCNT as acetone gas sensor. Sens Actuator A Phys. https://doi.org/10.1016/j.sna.2020.112240

[53] Liu C, Zhao L, Wang B et al (2017) Acetone gas sensor based on NiO/ZnO hollow spheres: fast response and recovery, and low (ppb) detection limit. J Colloid Interface Sci 495:207. https://doi.org/10.1016/j.jcis.2017.01.106

[54] Zhang Z, Wen Z, Ye Z, Zhu L (2015) Gas sensors based on ultrathin porous Co$_3$O$_4$ nanosheets to detect acetone at low temperature. RSC Adv 5:59976. https://doi.org/10.1039/c5ra08536e

[55] Song H, Yang H, Ma X (2013) A comparative study of porous ZnO nanostructures synthesized from different zinc salts as gas sensor materials. J Alloys Compd 578:272. https://doi.org/10.1016/j.jallcom.2013.05.211

Publisher's Note Springer Nature remains neutral with regard to jurisdictional claims in published maps and institutional affiliations.